Submitted to *Materials Science and Engineering A*

Hydrogen-assisted crack propagation in α-iron during elasto-plastic fracture toughness tests

Domas Birenis[a], Yuhei Ogawa[b,c], Hisao Matsunaga[d,e,f], Osamu Takakuwa[d,e,g]

Junichiro Yamabe[g,h], Øystein Prytz[a], Annett Thøgersen[i]

[a] *Department of Physics, Centre for Materials Science and Nanotechnology, University of Oslo, PO Box 1048 - Blindern, NO-0316 Oslo, Norway*

[b] *Graduate School of Engineering, Kyushu University, 744 Motooka, Nishi-ku, Fukuoka 819-0395, Japan*

[c] *Research Fellow of the Japan Society for the Promotion of Science, 744 Motooka, Nishi-ku, Fukuoka 819-0395, Japan*

[d] *Department of Mechanical Engineering, Kyushu University, 744 Motooka, Nishi-ku, Fukuoka 819-0395, Japan*

[e] *Research Center for Hydrogen Industrial Use and Storage (HYDROGENIUS), Kyushu University, 744 Motooka, Nishi-ku, Fukuoka 819-0395, Japan*

[f] *International Institute for Carbon-Neutral Energy Research (I2CNER), Kyushu University, 744 Motooka, Nishi-ku, Fukuoka 819-0395, Japan*

[g] *AIST-Kyushu University Hydrogen Materials Laboratory (HydroMate), 744 Motooka, Nishi-ku, Fukuoka 819-0395, Japan*

[h] *Department of Mechanical Engineering, Fukuoka University, 8-19-1 Nanakuma, Jonan-ku, Fukuoka 814-0180, Japan*

[i] *SINTEF Materials and Chemistry, PO Box 124 - Blindern, NO-0314 Oslo, Norway*

Abstract

Elasto-plastic fracture toughness tests of a commercially pure iron were performed in air and in hydrogen gas at two different pressures. Some unique characteristics of hydrogen-enhanced cracking were exhibited at both the macroscopic and microscopic length scales, based on the

observation of fracture surface, fracture plane, plasticity distribution and dislocation structure. The possible mechanisms responsible for the hydrogen-induced degradation of fracture toughness are discussed.

Keywords

Fracture toughness, hydrogen embrittlement, dislocation structures, electron back-scattered diffraction (EBSD), transmission electron microscopy (TEM)

1. Introduction

The reliability of structural materials in gaseous hydrogen environments is of great importance for realizing a hydrogen energy-based society. Ferritic steels with body-centered cubic (BCC) structures can be good alternatives to replace expensive metal alloys, such as are currently used in high-pressure hydrogen systems (*e.g.*, hydrogen refueling stations and fuel cell vehicles). It is commonly agreed that hydrogen deteriorates the mechanical properties of BCC steels, but a fundamental understanding of the underlying mechanisms remains elusive. A number of studies claim that hydrogen induces a premature failure, either due to enhanced localized plasticity (HELP) [1, 2], atomistic decohesion (HEDE) [3–6], adsorption-induced dislocation emission (AIDE) [7, 8] and/or hydrogen-enhanced strain-induced vacancy formation (HESIV) [9, 10]. Research has therefore been marked by long-lasting controversy. In addition, from a practical viewpoint, it is important to distinguish material performance under different loading conditions, whether monotonic or cyclic, taking into account various influencing factors (*e.g.*, hydrogen pressure, loading level, strain rate and temperature).

In order to elucidate the fundamental mechanism of hydrogen-induced cracking during cyclic loading, the authors recently conducted fatigue crack-growth (FCG) tests of a pure iron (*i.e.*, a

model system of BCC steels) in high-pressure hydrogen gas. Hydrogen was shown to cause significant FCG acceleration, at a rate some tens of times greater than the FCG rate in air, resulting in the formation of a quasi-cleavage (QC) type of fracture surface [11, 12]. After TEM observations of the dislocation structures immediately beneath the QC fracture surface, it was demonstrated that hydrogen had dramatically reduced the plasticity development level for crack propagation, triggering the fracture along a {001} plane. These results implied that, in the relatively high ΔK regime, where remarkable crack acceleration occurs, the micro-scale brittle cracking along the cleavage plane is an intrinsic mechanism for hydrogen-assisted cracking in BCC steels during cyclic loading. Additionally, the QC fracture surface was decorated by brittle-like striation markings and their spacing was consistent with a macroscopic FCG rate. The results indicated that the crack propagation was macroscopically stable, *i.e.,* it occurred on a cycle-by-cycle basis, even though the microscopic mechanism was seemingly unstable cleavage [12, 13].

In addition to the FCG properties, when performing a lifecycle assessment and a leak-before-break analysis for high-pressure hydrogen tanks and pipes, another important factor is the investigation of the effects of hydrogen on fracture toughness [14, 15]. In recent times, Ogawa *et al.* explored the similarities between the hydrogen-assisted crack propagation of a low-carbon steel during cyclic and monotonic loading, concluding that the intrinsic fracture mechanism was basically identical in both loading conditions [16]. They also determined that such embrittlement in fatigue and fracture toughness experiments was accompanied by substantial crack-tip sharpening and the formation of a QC fracture surface (*i.e.,* less crack-tip blunting), interpreting such phenomena based on the HELP hypothesis. Similar crack sharpening and quasi-brittle cracking in the presence of hydrogen have also been reported on Fe-Si single crystals subjected

to sustained or monotonic loading [4, 6, 17, 18]. For instance, Vehoff and Rothe [6] characterized the crack propagation behavior of Fe-2.6%Si single crystals in low-pressure gaseous hydrogen by measuring the crack-tip opening angle from the lateral surface of the specimen. They found that the crack propagated through a micro-scale repetition of alternating slip emission from the crack-tip and brittle cleavage, with the enhanced fraction of cleavage due to the presence of adsorbed hydrogen resulting in a substantially reduced crack-tip opening angle. A series of papers by Chen *et al.* [4, 17] suggested a decohesion-induced cleavage on a {100}-type plane of Fe-3%Si in hydrogen gas, even though a large amount of plasticity was observed at the crack-wake region in the *postmortem* samples. In these studies, Fe-Si alloys were used as representative samples of BCC crystals, due to the ease with which specimens with large grains and simple ferritic microstructures can be manufactured. However, Si is an important alloying element that affects the dislocation motion and fracture behavior in iron, enhancing planar slip and unexpected brittleness even without hydrogen [19, 20]. Indeed, Nakasato and Bernstein reported a difference in the crystal planes of hydrogen-induced transgranular cracks in pure iron and Fe-0.7~3%Si [21]. They demonstrated that the crack plane is always {011}, *i.e.*, a slip plane in pure iron, whereas in Fe-Si alloys, it shifts to a {001} plane with increasing silicon content. A similar tendency has been confirmed in other studies [22, 23], while some recent analyses have highlighted the importance of such hydrogen-assisted, slip-plane fracture, even in commercial BCC steels [24, 25]. These facts imply that Fe-Si alloys are not necessarily representative of the behaviors to be expected in conventional, structural BCC steels. Consequently, pure iron appears to be the better model material for clarifying the underlying fracture mechanisms that result from hydrogen exposure.

This study is a continuation of our previous research into the effect of a hydrogen gas

atmosphere on crack-growth resistance in commercially-pure, multi-crystalline iron [11–13]. In the present investigation, the hydrogen-induced degradation of elasto-plastic fracture toughness is explored. Some unique characteristics of the fracture morphology under the influence of hydrogen are exhibited, with the degradation mechanism discussed in terms of the fracture plane, the distribution of plastic deformation and the dislocation structures in the vicinity of the crack-tip.

2. Material and Experimental Methods

2.1 Material and specimens

The material used in this study was an annealed commercially-pure iron (JIS-C2504) with the chemical composition of 0.002%C-0.04%Mn-0.0004%P-0.0002%S. The material was received in the shape of a cylinder with a diameter of 80 mm. The yield stress, σ_{y}, and ultimate tensile strength, σ_{B}, were 140 MPa and 255 MPa, respectively. For the purpose of fracture toughness testing, compact tension (CT) specimens measuring 50.8 mm wide (width = *W)* and 14.9 mm thick (thickness = *B*) were cut from the cylinder, so that the loading direction lay parallel to the cylinder axis. Figure 1 displays the shape and dimensions of the CT specimens. In order to attain the plane-strain stress state throughout the entire crack-front, side grooves with a depth of 1.1 mm were machined on both sides of the specimens, *i.e.,* the net thickness of the specimens, B_N, was 12.7 mm.

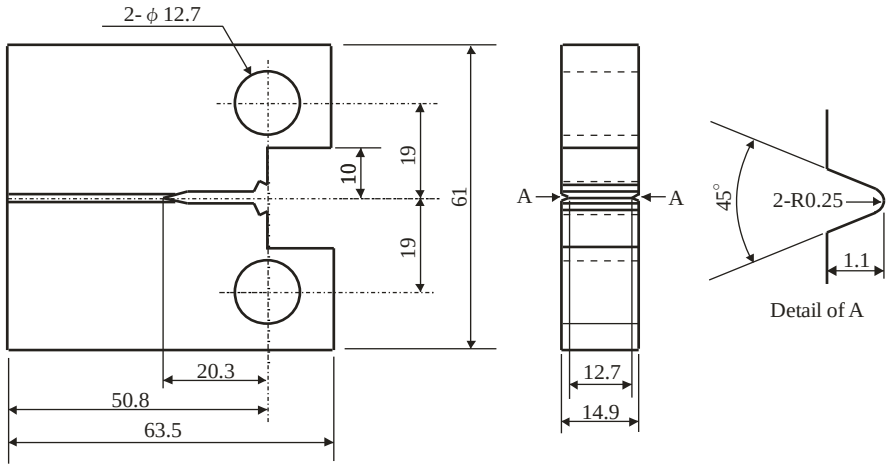

Fig. 1. Shape and dimensions of the CT specimens used for fracture toughness tests.

2.2 Fracture toughness testing

The elasto-plastic fracture toughness (J_{Ic}) tests were performed in laboratory air, as well as at 0.7 MPa- and 90 MPa-hydrogen gas at room temperature (RT). Servo-hydraulic testing machines equipped with hydrogen gas chambers were used for the tests. The purity of hydrogen gas was higher than 99.999%. The J_{Ic} tests reveal the relationship between *J* integral values and crack-extension length during monotonic loading (*J*-*R* curve), an effective way to assess the stability of macroscopic crack propagation. In this study, the tests were conducted in accordance with the resistance-curve procedure described in the ASTM-E1820 standard [26]. Based on this procedure, the CT specimens were loaded monotonically with iterative intermittent unloading cycles. The *J* values were determined according to the area below the load versus displacement curves. The displacement for this calculation is defined as crack mouth opening displacement (*COD*), which was measured by a clip-on gauge attached to the edge of the mechanical notch. The *J* value corresponding to the *i*-th loading-unloading sequence can be calculated according to the following equation:

$$J_{(i)} = \frac{K_{(i)}\left(1-\nu^2\right)}{E} + J_{pl(i)} \tag{1}$$

where the first and the second terms denote the elastic and plastic parts of the J integral respectively, E is elastic modulus, v is Poisson's ratio, and K is the stress intensity factor. The $K_{(i)}$ and $J_{pl(i)}$ parameters are calculated as follows:

$$K_{(i)} = \frac{P_i}{\sqrt{BB_N W}} \frac{\left[\left(2+{a_i}/{W}\right)\left(0.886+4.64\left({a_i}/{W}\right)-13.32\left({a_i}/{W}\right)^2+14.72\left({a_i}/{W}\right)^3-5.6\left({a_i}/{W}\right)^4\right)\right]}{\left(1-{a_i}/{W}\right)^{3/2}} \tag{2}$$

$$J_{pl(i)} = \left[J_{pl(i-1)} + \left(\frac{\eta_{(i-1)}}{b_{(i-1)}}\right)\frac{A_{pl(i)} - A_{pl(i-1)}}{B_N}\right]\left[1-\gamma_{(i-1)}\frac{a_{(i)} - a_{(i-1)}}{b_{(i-1)}}\right] \tag{3}$$

where a is crack length, b is ligament ($W-a$), A_{pl} is the plastic area under the P versus COD curves, η and γ are the geometrical factors defined as $\eta = 2.0+0.522b/W$ and $\gamma = 1.0 + 0.76b/W$ respectively. Meanwhile, the crack length, a, was monitored during the test progress from the elastic P-COD response of the specimens on each unloading line by using conventional unloading elastic compliance method.

2.3 Microscopic analyses

After the fracture toughness tests, the specimens were cut along the mid-thickness section: the lateral surface of one half was polished to a mirror-finish, while the other half was used for fractographic investigation, in combination with transmission electron microscopy (TEM) observation beneath the fracture surface. The polished side was analyzed using the FEI Quanta 3D scanning electron microscope (SEM), equipped with an electron back-scatter diffraction (EBSD) system by Oxford instruments, with the electron beam step size of 2 μm. Inverse pole figure (IPF) and grain-reference orientation deviation (GROD) maps were constructed to visualize the grain orientation and the degree of crystal rotation around the crack-tips. Electron-channeling contrast images (ECCIs) were also acquired by using a back-scattered electron detector at an acceleration voltage of 20 kV. Fracture surfaces were investigated using the same

SEM. TEM samples were extracted from the fracture surfaces with the help of a JEOL JIB-4500 Dual-beam machine, after a 2 μm-thick carbon layer was deposited in order to protect surface features from damage during milling. TEM samples were observed via FEI Titan G2 field-emission TEM, operated at 300 kV in scanning mode.

3. Results

3.1 Macroscopic reduction of crack-growth resistance by hydrogen

Figure 2(a) shows the load, *P*, vs. *COD* curves for specimens tested in air and in 0.7 MPa- and 90 MPa-hydrogen gas. In air, the value of *P* monotonically increased with an augmentation in *COD*. On the other hand, in hydrogen gas, the curves first deviated from those recorded in air at the *COD* of ≈ 1 mm and then plateaued. The *P* value in 90 MPa-hydrogen gas was lower than that in 0.7 MPa at equivalent *COD* values. Such a load decrease can be attributed to the successive crack propagation triggered by hydrogen [27], whereas large crack-blunting and corresponding strain-hardening are caused during the load increase in air, as will also be demonstrated in the latter part of this paper.

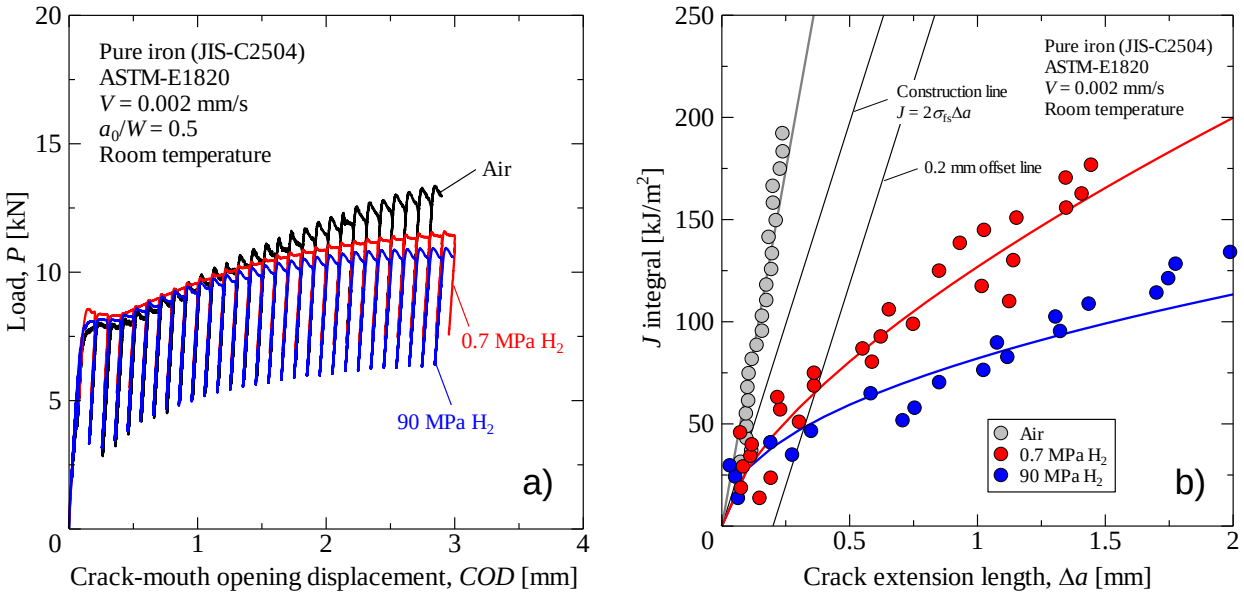

Fig. 2. (a) Relationship between the load and the crack-mouth opening displacement and (b) the corresponding crack-growth resistance curve (*J*-*R* curve) for specimens tested in air and in 0.7 MPa- and 90 MPa-hydrogen gas at room temperature.

The obtained results were used to construct the *J*-*R* curves presented in Fig. 2(b). This diagram illustrates the energy required for crack-blunting accompanied by strain-hardening, as well as for crack-extension. In Figure 2(b), a construction line is also depicted, determined as $J = 2\sigma_{fs}\Delta a$, where $\sigma_{fs} = (\sigma_y + \sigma_B)/2$ and Δa is the crack-extension length, as well as a 0.2 mm offset line of the construction line. The construction line corresponds to the crack-blunting line which represents the crack-tip opening displacement (*CTOD*), whereas the elasto-plastic fracture toughness value, J_{Ic}, is determined from the intersection of the *J*-*R* curve and the 0.2 mm offset line. Since all of the data points recorded in air were plotted on the left side of the construction line, this infers that in air, the crack was almost stationary and only crack-blunting occurred during testing. On the other hand, it is clearly visible that the cracks propagated successively in hydrogen gas, while absorbing much less energy, with the J_{Ic} values determined as 50 ~ 60

kJ/m^2. These J_{Ic} values in hydrogen gas were much higher than those in conventional BCC steels with 600 ~ 700 MPa of yield strength [28], supposedly owing to the lower yield stress of pure iron and the resultant larger plastic zone ahead of the crack-tip.

It is also important to note that, despite the degradation of fracture toughness in hydrogen gas compared to that in air, the slope of *J*-*R* curves, *i.e.*, tearing modulus (d*J*/d*a*), remained positive. Such a result indicates that the crack propagation is macroscopically stable. Conversely, it is known that in high-strength steels which show brittle, sub-critical, hydrogen-induced cracking, the *J*-*R* curve becomes horizontal [29].

3.2 Fracture surface morphologies

Figure 3 displays the fracture surfaces formed in air, as well as in 0.7 MPa- and in 90 MPa-hydrogen. The areas in the low magnification images (Figs. 3 (a) – (c)) correspond to regions located approximately 500 μm from the fatigue pre-crack front at the mid-thickness of the specimens. In the case of air, fine-striped patterns were observed perpendicular to the overall crack-growth direction (CGD), as presented in Fig. 3(d), representing the formation of the stretch zone due to large crack-blunting. Otherwise, in the case of hydrogen gas, as shown in Figs. 3(e) and 3(f), cleavage-like features (*i.e.*, quasi-cleavage) were detected throughout the fractured surface. The local CGD varied in different grains and could be determined from the direction of the river patterns. In addition, three types of characteristic striated markings were identified covering the quasi-cleavage fracture surfaces:

I. Narrowly-spaced markings (*viz.* yellow arrows in Figs. 3(e) and 3(f)) ─ The markings were perpendicular to the local CGD, with spacings of ≈1 μm in the case of 0.7 MPa-hydrogen gas and of ≈5 μm in the case of 90 MPa-hydrogen gas.

II. Widely-spaced markings (*viz.* blue arrow in Fig. 3(f)) ─ The markings were observed in the case of 90 MPa-hydrogen gas. These markings were spaced at ~80 μm, implying that they had formed during the loading-unloading cycle.

III. Widely-spaced markings (*viz.* red arrows in Fig. 3(e)) ─ The markings were observed in the case of 0.7 MPa-hydrogen gas. This type of marking was somewhat different from Type II. Several sets of sharp lines were oriented at different angles with respect to each other and randomly oriented to the local CGD.

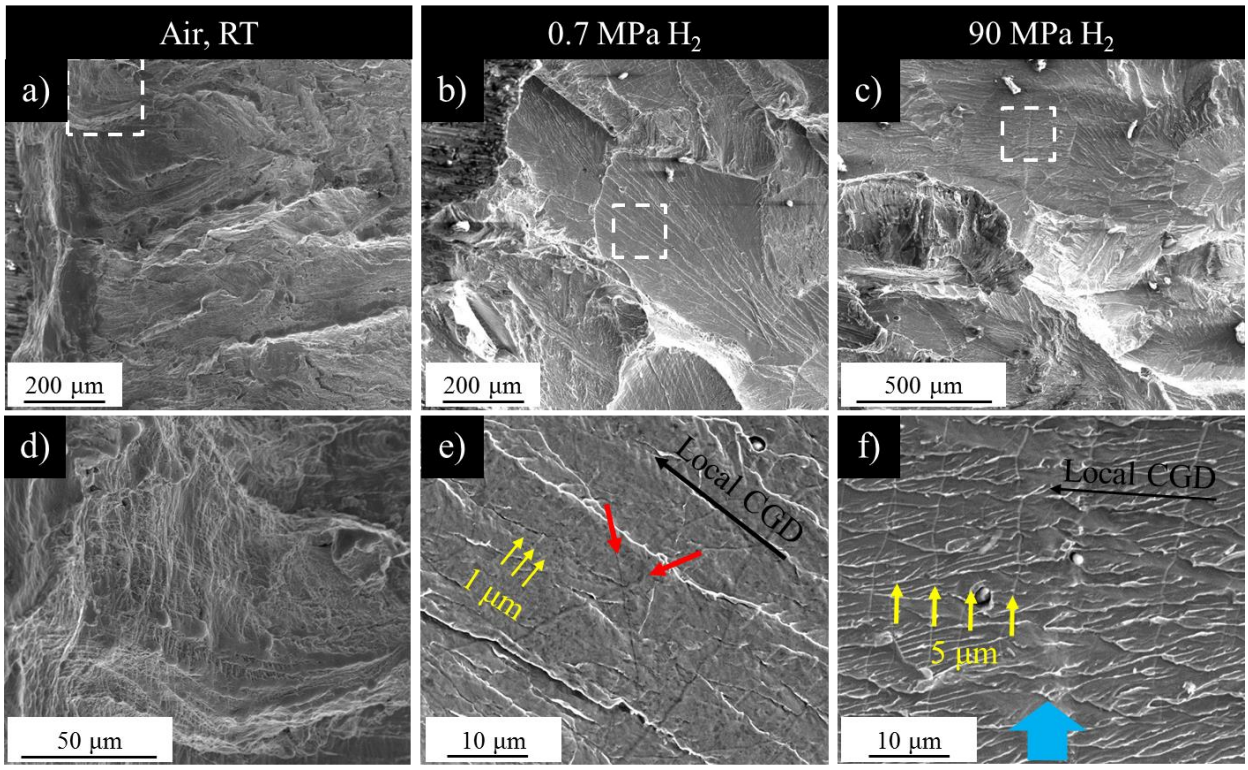

Fig. 3. Fracture surfaces of the specimens tested in air, (a) and (d); 0.7 MPa-hydrogen gas, (b) and (e); and 90 MPa-hydrogen gas, (c) and (f). Dashed rectangles in (a) – (c) outline the positions of (d) – (f), respectively. The overall crack-growth direction is from right to left and local crack-growth directions are indicated with black arrows. Yellow arrows identify the

narrowly-spaced striations in 0.7 MPa- and 90 MPa-hydrogen gas. The red and blue arrows mark the widely-spaced striations formed in 0.7 MPa- and 90 MPa-hydrogen gas, respectively.

EBSD-GROD maps as well as grain orientation maps were acquired from the lateral surfaces of all specimens, in order to compare the differences in overall plastic deformation amongst the various samples. As is evident in Fig. 4, there was a distinct difference in the shape of the cracks, depending on the particular testing environments. While samples tested in air possessed large crack-opening angles and blunted crack-tips, specimens tested in hydrogen had much smaller crack-openings and substantially sharper tips. The crack paths in all three samples were found to be transgranular. In the case of air, the crack was heavily deformed, and it was not possible to define the crystallographic crack path. In comparison, in hydrogen gas, the material around the cracks was only slightly deformed and the paths were almost straight across individual grains. These differences are clearly reflected on the GROD maps, where pronounced crystal rotation is visible around the crack-tip in the case of air (Fig. 4(d)). In hydrogen gas, the degree of crystal misorientation is markedly reduced, as can be observed in Figs. 4(e) and 4(f). In Figs. 4(b) and 4(c), the orientation of some individual grains is depicted by unit cell figures, in order to predict the orientation of the fracture planes. In the case of 0.7 MPa-hydrogen gas, the fracture-plane projections for all of the analyzed grains seem to be parallel to the {100} plane, as evidenced in Fig. 4(b). In comparison, in the case of 90 MPa-hydrogen gas, the fracture-plane traces match with different planes. The crack-plane trace in the grain marked “A” seemingly matches the {211} plane. Additionally, in grain “B”, it is also close to the {211} plane, but with slight misorientation. In grain “C”, the crack-plane trace is parallel to the {100} plane and, in grain “D”, a quite well-defined {110} trace can be matched to the crack plane. However, such an

analysis does not present the complete picture, since EBSD images provide cross-sectional views of three-dimensional samples. Crack lines are therefore only projections of fracture planes.

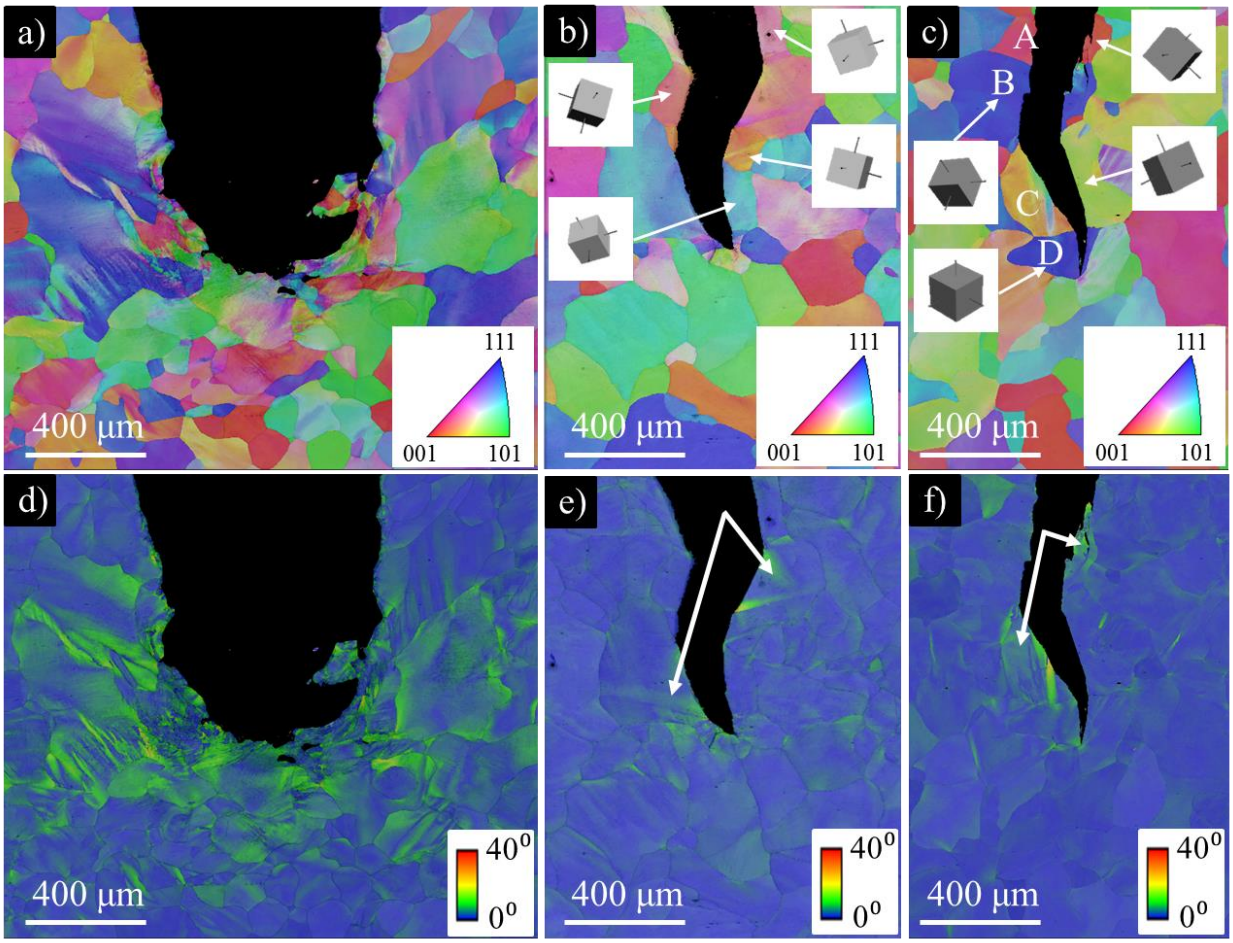

Fig. 4. EBSD IPF (a) – (c) and GROD (d) – (f) maps of the mid-thickness fracture paths in air, (a) and (d); in 0.7 MPa-hydrogen gas, (b) and (e); and in 90 MPa-hydrogen gas, (c) and (f).

In order to visualize the macro-scale deformation sub-structures, ECCIs were obtained in the same regions as in Fig. 4. Figures 5 (a) – (c) represent low magnification overview micrographs and Figs. 5 (d) – (f) are higher magnification micrographs near the crack-tips. The deformation magnitude is emphasized in Figs. 5 (a) – (c). In the case of air, a heavy plastic deformation resulted in a blurry channeling contrast. In comparison, in hydrogen gas, the microstructural

features are clear away from the crack, but more distortion is visible in the region closer to the crack. White dashed lines in Fig. 5(d) identify two sets of deformation bands that had formed along shear directions. They actively contributed to the crack-blunting, accompanied by the formation of the stretch zone. Conversely, Figs. 5(e) and 5(f) display rather clean microstructures around the crack-tips, with the formation of dislocation structures appearing less pronounced as compared with in air. Included in the micrographs are some references to dislocation boundaries, composed of either a cell-block boundary or a domain boundary [30, 31], *i.e.*, geometrically-necessary boundaries. In the case of 0.7 MPa-hydrogen gas, the crack-path is not as straight as in the case of 90 MPa-hydrogen gas, where the crack-path is significantly straighter in two neighboring grains, with a slight deviation after crossing a grain boundary (red dashed line), as seen in Fig. 5(f).

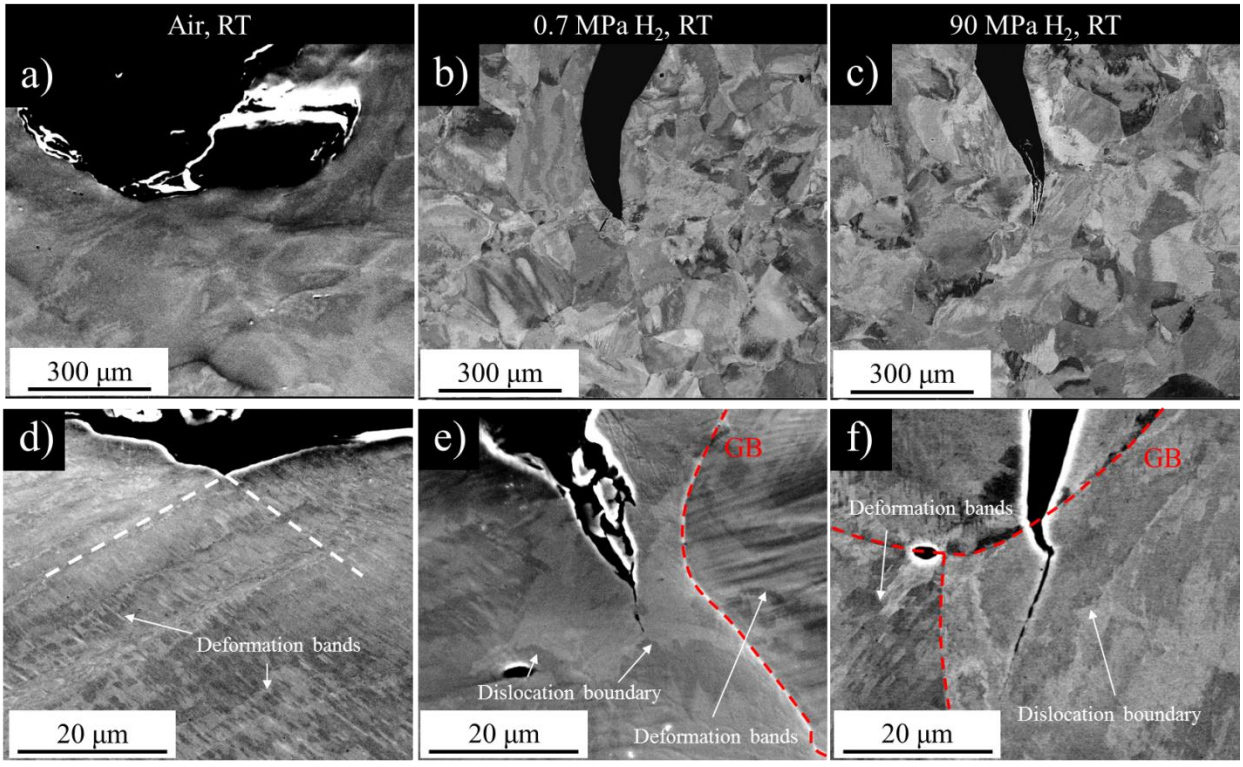

Fig. 5. ECCIs of the mid-thickness fracture paths in air, (a) and (d); in 0.7 MPa-hydrogen gas, (b) and (e); and in 90 MPa-hydrogen gas, (c) and (f). The crack-growth direction is from top to bottom.

Transmission electron microscopy in a scanning mode (STEM) was employed in order to image dislocation structures at a higher spatial resolution. Since the specimen tested in air had a blunt and stationary crack-tip, it was not technically feasible to extract FIB lamellae from its fracture surface, due to substantial surface inclination. As a result, STEM imaging was not performed on the sample fractured in air. STEM micrographs, as well as SEM micrographs of the corresponding positions of TEM lamellae extracted from the fracture surfaces formed in 0.7 MPa- and 90 MPa-hydrogen gas, are presented in Fig. 6. The regions from which the TEM samples were extracted were representative of typical quasi-cleavage fracture.

Regarding the specimen tested in 0.7 MPa-hydrogen gas, as displayed in Fig. 6(a), the extracted TEM sample bore sharp, widely-spaced, crisscrossing striations (Type III), interspersed with blurry, narrowly-spaced striations (Type I) which are not visible in the image due to low magnification. The widely-spaced striations are visible in the STEM micrograph as small steps (*viz.* the white arrow in Fig. 6(b)). Clearly, such striations correspond to the dislocation walls that run obliquely to the fracture surface. The diffraction pattern in the inset reveals that the fracture surface is parallel to the {100} plane, while the dislocation wall lies parallel to the {111} plane. In addition, in Fig. 6(b), two sets of bands can be distinguished, as indicated by red and white arrows. It would appear that the set identified by the red arrows had formed first, only to be subsequently sheared off by the band marked with the white arrow. The dislocation structure beneath the fracture surface is comprised of densely-scattered dislocation tangles. Taken from

the region outlined by a dashed square in Fig. 6(b), the higher magnification image in Fig. 6(c) does not reveal the presence of any well-developed dislocation cells or sub-grains, even immediately beneath the fracture surface. The narrowly-spaced striations, indicated with yellow arrows in Fig. 3(e), are not resolved in Fig. 6(a), but traces of them remain visible as small bumps in the TEM micrograph (yellow arrows in Fig. 6(c)). There are no particular dislocation structures beneath them.

Two TEM samples were extracted from the fracture surface of the specimen tested in 90 MPa-hydrogen — one from a region with narrowly-spaced striations (Type I), and the other from a region of widely-spaced striations (Type II), as shown in Figs. 6(d) and 6(g). The narrowly-spaced markings correspond to steps, as exhibited in Fig. 6(e). The dislocation band seen in the micrograph is visible solely beneath that particular step, while only dislocation tangles are observed beneath the other steps. The higher magnification image in Fig. 6(f) unveils an increased density of dislocations in the region of 200 – 300 nm depth beneath the fracture surface. However, converged-beam diffraction revealed smooth-angle variation when moving electron beam along the surface, or from the surface to deeper into the sample. This indicates that the high density of dislocations is stored statistically, without the formation of any dislocation boundaries that may bear a substantial misorientation angle [32]. The diffraction pattern in the inset of Fig. 6(e), taken from the sample edge, highlights rather sharp diffraction spots with no splitting or streaking, confirming the absence of an evolved dislocation structure. Furthermore, it was revealed that the fracture surface plane lay parallel to the {211} plane, as shown in the inset of Fig. 6(e). An increased density of the dislocation walls could be observed beneath each widely-spaced band, as represented by red arrows in Fig. 6(h). This phenomenon indicates that a considerable amount of plasticity had been introduced during each loading cycle.

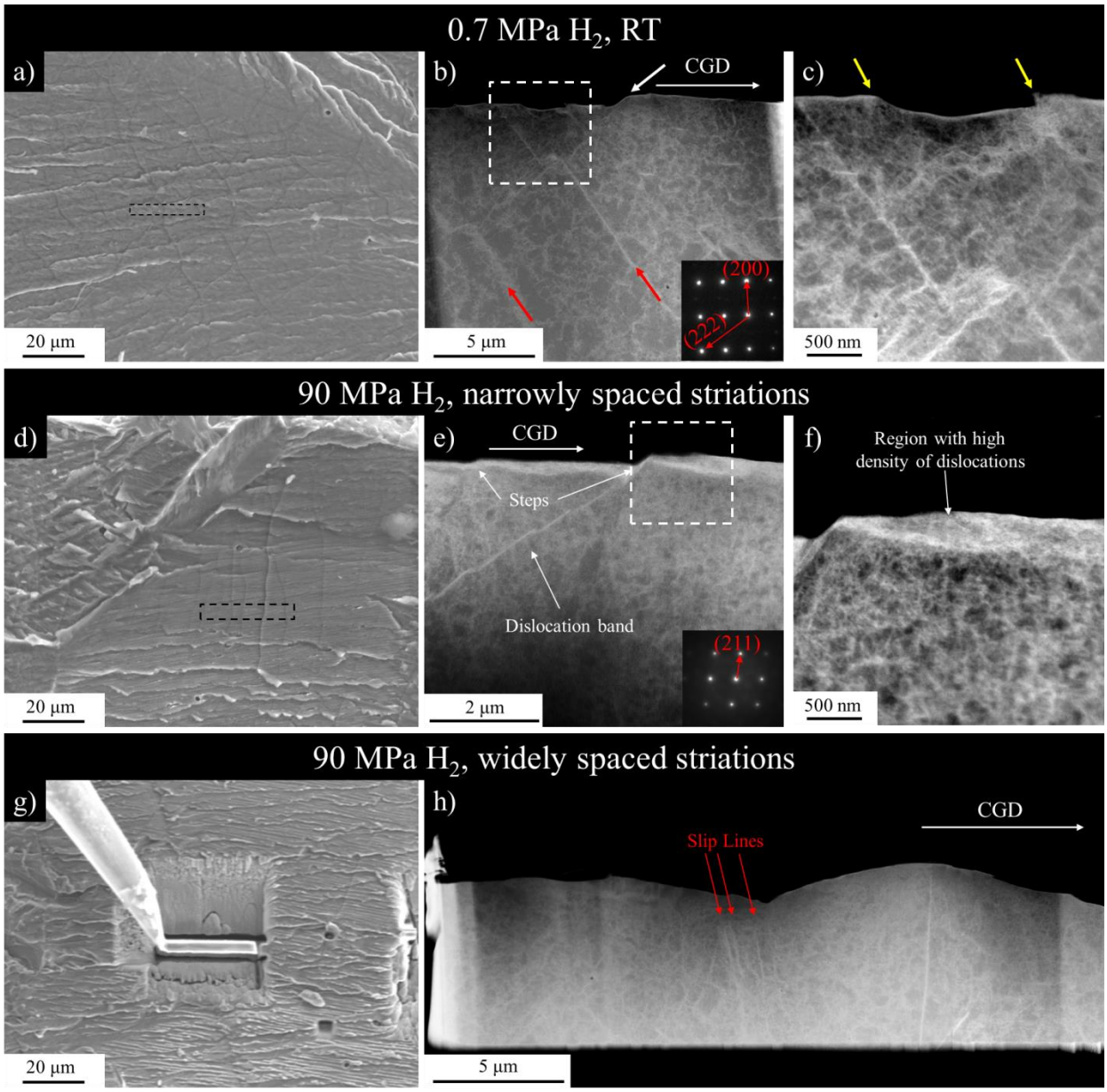

Fig. 6. FIB lift-out locations and dark-field STEM micrographs of samples fractured in 0.7 MPa-hydrogen gas, (a) – (c); and 90 MPa-hydrogen gas, (d) – (h). Micrographs in (c) and (f) are taken from the dashed regions in (b) and (e), respectively. Crack growth direction runs from left to right.

4. Discussion

4.1 Fractography and striations/crack-arrest markings

As already documented in existing studies of hydrogen embrittlement in iron-based BCC alloys [4, 21, 33], failure in a gaseous hydrogen environment accompanied the QC-type fracture features in our J_{Ic} tests of pure iron. Intrinsic features of the QC fracture included the existence of river patterns running parallel to the local CGD, as well as striation-like patterns lying perpendicular to the river patterns. Such striations tend to form on a cycle-by-cycle basis in the context of fatigue cracks. This means that during each loading cycle, the crack-tip grows a certain distance and then gets arrested and blunted until the next loading cycle [34, 35]. Accordingly, striation-spacing roughly corresponds to the macroscopic crack-growth rate. Similar markings were also observed in our J_{Ic} tests, as well as in the sustained-load experiments conducted by other researchers [4, 33] and referred to as "crack-arrest markings" [36].

In our experiments, the distances between the crack-arrest markings were dependent on hydrogen pressure (*i.e.*, ≈1 μm at 0.7 MPa and ≈5 μm at 90 MPa). This variation in distance can be interpreted with respect to hydrogen concentration and distribution. At a higher hydrogen pressure, more hydrogen can diffuse from the crack-tip into the material. As a result, a larger volume ahead of the crack-tip can contain a critical amount of hydrogen, such as is required to trigger a QC-type fracture. This, in turn, can cause longer crack propagation steps during the loading cycle. In this study, the mechanism behind the formation of crack-arrest markings has not been clarified in detail. Nonetheless, it is commonly agreed that crack propagation occurs via a discontinuous crack-front advancement, as supported by acoustic emission experiments [4, 33]. However, there exist no experimental observations which document exactly how these patterns form and the precise mechanism remains unclear.

Other sets of widely-spaced markings were observed on the fracture surfaces of samples tested in hydrogen gas. However, the striation morphologies were different between 0.7 MPa and 90 MPa. At 0.7 MPa, there were multiple sets of widely-spaced markings (Type III), oriented at random angles with respect to each other and to the overall CGD (*c.f.* red arrows in Fig. 3(e)). Since it is unlikely that such features could have formed during the discontinuous crack propagation process, they are therefore assumed to result from slip activities operating in the crack-wake during the later loading cycles. This outcome is of little importance in the context of the fracture processes. The same assertion applies with regard to widely-spaced striations observed in samples tested in 90 MPa of hydrogen (Type II). All of the dislocation walls beneath the fracture surfaces were attributed to the formation of these striations and not to the crack-arrest markings. In consequence, these markings have no determining role in the crack-growth process.

4.2 Crystallography

In our previous research about FCG in the same pure-grade iron [12], we concluded that crack acceleration in fatigue experiments was mainly caused by the fracture along the {100} cleavage plane, with such cleavage fracture assumed to be a consequence of the reduced mobility of the dislocations around the crack-tip. Even in the present study, the fracture along the {100} plane was clearly visible in 0.7 MPa-hydrogen gas. However, EBSD and TEM diffraction results showed that in the case of 90 MPa-hydrogen gas, the fracture planes were parallel to {211} or {110}, *i.e.*, slip planes in BCC crystal, with the combination of {100}-type fracture. This result may imply that, at higher hydrogen pressures, the greater amount of hydrogen leads to a reduction of bonding energy. As such, even lower energy planes can be separated due to

atomistic decohesion, if they are oriented more favorably with respect to the loading direction. Indeed, Hinotani *et al.* showed that notched, pure iron single crystal, oriented so that its loading axis was along a <100> direction, was seen to fracture along a (100) plane with a minimal amount of deformation. In contrast, when its loading axis was oriented along a <110> direction, the crack grew along a (110) plane with a significant amount of plasticity [37]. Similar results were also obtained by Kimura *et al.* [38]. Furthermore, if the dislocations distribute on the slip planes, it is expected that the matrix bonding of such planes is reduced because of the lost integrity of the crystal structure, as suggested by Gilman [39], thus making the slip planes the preferable path for the fracture. Matsumoto *et al.* elegantly demonstrated such a type of fracture by using molecular dynamics calculations, also proposing that the hydrogen trapped at the dislocation core on a (110) slip plane assists in the final separation of the slip plane via HEDE [40]. However, in order to reinforce these hypotheses, it is necessary to obtain a statistically-significant amount of data. In this regard, since the EBSD and TEM techniques are not practical, further studies using other techniques are required to support these assumptions.

4.3 Plastic deformation distribution and dislocation structures

The low magnification ECCIs (Figs. 5(a) – (d)) which display the overall microstructure of the specimens, supply information similar to the IPF images (Figs. 4(a) – (d)). For example, in the specimen fractured in air, a diffuse and blurry channeling contrast near the crack-tip can be explained by the lost microstructural integrity that resulted from substantial plastic deformation. The same conclusion can be derived from the corresponding IPF image (Fig. 4(a)), where the grain boundaries do not present as sharp borders between the grains, but rather exhibit smooth transitions with almost indistinguishable boundary. Features that are more interesting are

resolved at higher magnifications (Figs. 5(d) – (f)). Namely, in the case of air, a dense distribution of deformation bands is visible due to their different contrasts. Two overall band directions can be distinguished (white dashed lines); it is easy to visualize the crack-blunting because of the continuous alternating shear on these two deformation bands. In contrast, the specimens fractured in hydrogen gas possess much cleaner microstructures, with clearly visible grain boundaries and only slight contrast variations across individual grains. Similar observations were recorded during our previous fatigue experiments [12, 13], demonstrating that the fundamental embrittlement mechanism does not change between the fracture toughness crack and the fatigue crack. This has also been discussed by Ogawa *et al.* in their evaluation of the fatigue and fracture toughness performance of a carbon steel in a gaseous hydrogen environment [16].

Notwithstanding, the majority of the previous studies have confirmed plasticity localization in materials fractured under various loading conditions in a hydrogen atmosphere [2, 41, 42]. In such cases, heavily-evolved, nano-sized sub-grains, or even an amorphous phase, have been detected underneath the fracture path [42–44]. Even though we discovered a higher density of dislocations in the zone just beneath the fracture surface formed in 90 MPa-hydrogen gas (Fig. 6(f)), they established no advanced dislocation structures, but instead distributed quite randomly. This means that in comparison to the specimen tested in air, where substantially-developed deformation bands were identified, the level of plasticity development was reduced in hydrogen gas. This can be attributed to (i) fracture at a lower plastic strain than in air and/or, (ii) hydrogen-induced dislocation locking.

The former hypothesis (*i.e.*, fracture at a lower plastic strain) can be related to either the HEDE mechanism, by which hydrogen reduces the bonding strength of the matrix atoms [45,

46], or the AIDE mechanism [8], via which hydrogen adsorption onto the crack surfaces facilitates the dislocation nucleation from the crack-tip, leading to accelerated crack-growth through easier slip. In the case of AIDE, the crack-tip dislocation sources are activated prior to the extensive dislocation activity that occurs ahead of the crack-tip. The strain expansion from the crack-tip is then significantly reduced, thereby inhibiting severe crack-blunting, as shown in Figs. 4(b) and 4(c), or 4(e) and 4(f). This could cause enhanced crack-growth, as well as underdeveloped dislocation structures beneath the fracture surface.

Based on the latter hypothesis (*i.e.*, hydrogen-induced dislocation locking), the hydrogen trapped at the dislocation core can act as an obstacle for the movement of edge dislocations, as well as the sideward motion of kink pairs on screw dislocations. In such a case, the plastic relaxation at the crack-tip is suppressed and the material will then prematurely fail in a brittle manner. If the motion of the screw dislocations is inhibited by hydrogen in the crack-tip zone [47], the formation of dislocation cells or deformation band structures becomes difficult, due to the reduction of cross-slip ability, *i.e.*, three-dimensional mobility of dislocations. This hypothesis can rationalize the structural configuration observed in Fig. 6(f). Specifically, even though a high density of dislocations is introduced through the emission from the crack-tip, it is difficult for their distribution to be rearranged in low-energy configurations (*e.g.*, cells or low-angle tilt boundaries) [31], resulting in the lack of evolved structure.

As already mentioned, most previous research placed emphasis on the HELP model in an attempt to explain crack propagation behavior in a hydrogenating environment. It was thus assumed that the fracture mechanism was essentially the same as that present in an inert environment, but that it was simply localized in the crack-tip zone [2, 42, 44, 48]. Such an assumption has been thoroughly supported by critical evidence which has demonstrated that

absorbed hydrogen enhances dislocation mobility, generation and multiplication, thereby accelerating crack-tip plasticity in *in-situ* TEM straining experiments [49–51]. However, if purely localized ductile fracture is the sole mechanism for all types of hydrogen-related fracture, there seems to be no reason for the crack to propagate selectively along some specific low-index planes, *e.g.*, {001}, {011}. All of our present results suggest that the cohesion along those specific crystal planes becomes the weakest link in the presence of hydrogen, with the material suffering from premature separation, assisted by the afore-mentioned reduction of screw dislocation mobility and the resultant difficulty of plastic relaxation. This theory can also be supported by the fact that cracking has been reported along the {001} or {011} planes during severe hydrogen charging, even without externally-applied stress [21, 22]. As was the case with previous research, the present investigation also failed to elucidate the reason for such selective fracture along those specific planes.

5. Conclusions

Gaseous hydrogen-induced embrittlement in a pure Fe at room temperature during elasto-plastic fracture toughness tests was manifested by brittle-like fracture surface features, as well as substantial changes in the deformation substructures around the crack-tip zone and the crack-wake. The key findings in the present study are summarized as follows:

1. The crack propagated while absorbing much less energy, *i.e.*, the crack-growth resistance (*J-R*) curves were degraded in hydrogen gas environments. However, even in such a case, the slope of *J-R* curves was positive in all environmental conditions, concluding that the cracks still grew in a stable manner under a macroscopic view.

2. The reduction of crack-growth resistance was accompanied by quasi-cleavage fracture, regardless of the hydrogen gas pressure. Additionally, crack-tips in specimens, which had fractured in hydrogen gas, were significantly sharper, with a minimal amount of blunting, while the cracks produced in air were heavily blunted and hardly propagated.
3. The quasi-cleavage fracture surface in hydrogen gas was decorated with striation patterns perpendicular to the crack-growth direction (*i.e.* crack-arrest markings), implying that the cracks in hydrogen gas propagated intermittently during the loading steps. The spacings between these markings were larger at higher hydrogen pressures.
4. EBSD analyses exposed evolved deformation substructures around the crack-tip in air, due to the establishment of deformation bands or other types of geometrically-necessary boundaries with a high misorientation angle. However, such crystal rotation was barely detected in the case of the crack which had propagated in hydrogen gas.
5. TEM observations revealed no evolved dislocation structures beneath the fracture surface formed in hydrogen gas, regardless of the crystallographic orientation of the fracture plane. Rather, it demonstrated a random distribution of redundant dislocations, as well as a few dislocation walls with negligible misorientation angles.

The findings suggest that the cracks in hydrogen propagated with less development of plasticity as opposed to localized plasticity, even in the immediate vicinity of the fracture path. This conclusion is consistent with our previous investigation into hydrogen-assisted, fatigue crack growth in pure iron, demonstrating also that the intrinsic mechanism of crack propagation is the same in both cyclic and monotonic loading.

Acknowledgements

This work was supported by JSPS KAKENHI (Grant Nos. JP16H04238 and JP16J02960). The Research Council of Norway is acknowledged for its support through the Norwegian Center for Transmission Electron Microscopy, NORTEM (Grant No. 197405/F50). This study also forms part of the "HIPP" project from the PETROMAKS2 program, funded by the Research Council of Norway (Grant No.102006899).

Data availability

The raw/processed data required to reproduce these findings cannot be shared at this time as the data also forms part of an ongoing study.

References

[1] S. Wang, M. L. Martin, P. Sofronis, S. Ohnuki, N. Hashimoto, and I. M. Robertson, Acta Mater. **69**, 275 (2014).

[2] M. L. Martin, J. A. Fenske, G. S. Liu, P. Sofronis, and I. M. Robertson, Acta Mater. **59**, 1601 (2011).

[3] T. J. Marrow, P. J. Cotterill, and J. E. King, Acta Metall. Mater. **40**, 2059 (1992).

[4] X. Chen and W. W. Gerberich, Metall. Trans. A **22**, 59 (1991).

[5] H. Vehoff and P. Neumann, Acta Metall. **28**, 265 (1980).

[6] H. Vehoff and W. Rothe, Acta Metall. **31**, 1781 (1983).

[7] S. P. Lynch, Acta Metall. **36**, 2639 (1988).

[8] S. Lynch, Corros. Rev. **30**, (2012).

[9] M. Nagumo, Mater. Sci. Technol. **20**, 940 (2004).

[10] K. Takai, H. Shoda, H. Suzuki, and M. Nagumo, Acta Mater. **56**, 5158 (2008).

[11] Y. Ogawa, D. Birenis, H. Matsunaga, O. Takakuwa, J. Yamabe, Ø. Prytz, and A. Thøgersen, Mater. Sci. Eng. A **733**, 316 (2018).

[12] D. Birenis, Y. Ogawa, H. Matsunaga, O. Takakuwa, J. Yamabe, Ø. Prytz, and A. Thøgersen, Acta Mater. **156**, 245 (2018).

[13] Y. Ogawa, D. Birenis, H. Matsunaga, A. Thøgersen, Ø. Prytz, O. Takakuwa, and J. Yamabe, Scr. Mater. **140**, 13 (2017).

[14] KHK, *KHKS 0220, KHK Standard for Pressure Equipment Containing Ultrahigh Pressure Gas.* (Tokyo, 2010).

[15] ASME, *ASME Boiler and Pressure Vessel Code Section VIII, Division 3, Article KD-10* (2010).

[16] Y. Ogawa, H. Matsunaga, J. Yamabe, M. Yoshikawa, and S. Matsuoka, Int. J. Fatigue **103**, 223 (2017).

[17] X. Chen, T. Foecke, M. Lii, Y. Katz, and W. W. Gerberich, Eng. Fract. Mech. **35**, 997 (1990).

[18] T. J. Marrow and J. E. King, Fatigue Fract. Eng. Mater. Struct. **17**, 761 (1994).

[19] D. Caillard, Acta Mater. **61**, 2793 (2013).

[20] D. Caillard, Acta Mater. **61**, 2808 (2013).

[21] F. Nakasato and I. M. Bernstein, Metall. Trans. A **9**, 1894 (1978).

[22] A. S. Tetelman and W. D. Robertson, Acta Metall. **11**, 415 (1963).

[23] A. Inoue, Y. Hosoya, and T. Masumoto, Tetsu-to-Hagane **65**, 525 (1979).

[24] A. Shibata, Y. Momotani, T. Murata, T. Matsuoka, M. Tsuboi, and N. Tsuji, Mater. Sci. Technol. **33**, 1524 (2017).

[25] A. Nagao, C. D. Smith, M. Dadfarnia, P. Sofronis, and I. M. Robertson, Acta Mater. **60**, 5182 (2012).

[26] ASTM, *ASTM E1820, Standard Test Method for Measurement of Fracture Toughness* (West Conshohocken, PA, 2009).

[27] S. Matsuoka, J. Yamabe, and H. Matsunaga, Eng. Fract. Mech. **153**, 103 (2016).

[28] C. San Marchi and B. P. Somerday, *Technical Reference for Hydrogen Compatibility of Materials* (Albuquerque, 2012).

[29] K. A. Nibur, B. P. Somerday, C. S. Marchi, J. W. Foulk, M. Dadfarnia, and P. Sofronis, Metall. Mater. Trans. A **44**, 248 (2013).

[30] B. Bay, N. Hansen, D. A. Hughes, and D. Kuhlmann-Wilsdorf, Acta Metall. Mater. **40**, 205 (1992).

[31] D. Kuhlmann-Wilsdorf, Mater. Sci. Eng. A **113**, 1 (1989).

[32] D. . Hughes, N. Hansen, and D. . Bammann, Scr. Mater. **48**, 147 (2003).

[33] T. J. Marrow, M. Aindow, P. Prangnell, M. Strangwood, and J. F. Knott, Acta Mater. **44**, 3125 (1996).

[34] H. Nishikawa, Y. Oda, and H. Noguchi, J. Solid Mech. Mater. Eng. **5**, 370 (2011).

[35] J. Yamabe, M. Yoshikawa, H. Matsunaga, and S. Matsuoka, Int. J. Fatigue **102**, 202 (2017).

[36] S. P. Lynch, Mater. Sci. Eng. A **468**–**470**, 74 (2007).

[37] S. Hinotani, Y. Ohmori, and F. Terasaki, Mater. Sci. Technol. **10**, 141 (1994).

[38] A. Kimura and H. Kimura, Mater. Sci. Eng. **77**, 75 (1986).

[39] J. J. Gilman, J. Appl. Phys. **32**, 738 (1961).

[40] R. Matsumoto, S. Taketomi, S. Matsumoto, and N. Miyazaki, Int. J. Hydrogen Energy **34**, 9576 (2009).

[41] S. Wang, A. Nagao, K. Edalati, Z. Horita, and I. M. Robertson, Acta Mater. **135**, 96 (2017).

[42] S. Wang, A. Nagao, P. Sofronis, and I. M. Robertson, Acta Mater. **144**, 164 (2018).

[43] M. Nagumo, T. Ishikawa, T. Endoh, and Y. Inoue, Scr. Mater. **49**, 837 (2003).

[44] T. Neeraj, R. Srinivasan, and J. Li, Acta Mater. **60**, 5160 (2012).

[45] R. A. Oriani, Annu. Rev. Mater. Sci. **8**, 327 (1978).

[46] A. R. Troiano, Metallogr. Microstruct. Anal. **5**, 557 (2016).

[47] H. Matsui, H. Kimura, and A. Kimura, Mater. Sci. Eng. **40**, 227 (1979).

[48] T. Tabata and H. K. Birnbaum, Scr. Metall. **18**, 231 (1984).

[49] P. J. Ferreira, I. M. Robertson, and H. K. Birnbaum, Acta Mater. **46**, 1749 (1998).

[50] T. Tabata and H. K. Birnbaum, Scr. Metall. **17**, 947 (1983).